Journal of Archaeological Science 57 (2015) 380–394

Contents lists available at ScienceDirect

Journal of Archaeological Science

journal homepage: http://www.elsevier.com/locate/jas

Technical considerations and methodology for creating high-resolution, color-corrected, and georectified photomosaics of stratigraphic sections at archaeological sites

Erich C. Fisher [a, *], Derya Akkaynak [b, c, d, 1], Jacob Harris [a, 1], Andy I.R. Herries [e, 1], Zenobia Jacobs [g, 1], Panagiotis Karkanas [f, 1], Curtis W. Marean [a, h, 1], James R. McGrath [i, 1]

[a] Institute of Human Origins, School of Human Evolution and Social Change, Arizona State University, Tempe, AZ 85287-2402, USA
[b] Department of Mechanical Engineering, Massachusetts Institute of Technology, 77, Massachusetts Avenue, Cambridge, MA 02139, USA
[c] Applied Ocean Science and Engineering, Woods Hole Oceanographic Institution, 266 Woods, Hole Road, Woods Hole, MA 02543, USA
[d] Program in Sensory Physiology and Behavior, Marine Biological Laboratory, 7 MBL Street, Woods Hole, MA 02543, USA
[e] Australian Archaeomagnetism Laboratory, Department of Archaeology, Environment and Community Planning, La Trobe University, Melbourne Campus, Bundoora 3086, VIC, Australia
[f] Malcolm H. Wiener Laboratory for Archaeological Science, American School of Classical Studies, Souidias 54, Athens 10676, Greece
[g] Centre for Archaeological Science, School of Earth and Environmental Sciences, University of Wollongong, Northfields Avenue, Wollongong, New South Wales, 2522, Australia
[h] Faculty of Science, Nelson Mandela Metropolitan University, Port Elizabeth, Eastern Cape 6031, South Africa
[i] Department of Anthropology, University of Iowa, 114 Macbride Hall, Iowa City, IA 52242, USA

ARTICLE INFO

Article history:
Received 22 April 2014
Received in revised form
21 January 2015
Accepted 3 February 2015
Available online 10 March 2015

Keywords:
Archaeoinformatics
Digital photography
Modern human origins
South Africa

ABSTRACT

Using a conventional, off-the-shelf digital single lens reflex camera and flashes, we were able to create high-resolution panoramas of stratigraphic profiles ranging from a single meter to over 5 m in both height and width at the Middle Stone Age site of PP5-6 at Pinnacle Point, Mossel Bay, South Africa. The final photomosaics are isoluminant, rectilinear, and have a pixel spatial resolution of 1 mm. Furthermore, we systematically color-corrected the raw imagery. This process standardized the colors seen across the photomosaics while also creating reproducible and meaningful colors for relative colorimetric analysis between photomosiacs.

Here, we provide a detailed discussion about the creation and application of our photomosaics. In the first part of the paper, we examine the specific characteristics of modern digital single lens reflex (DSLR) cameras and lenses that were important to us in developing our methodology. We also provide a detailed discussion about how to reproduce the methodology in the field and to post-process the imagery. In the final section of the paper, we give several examples to show how we apply our photomosaics within an empirical 3D GIS database. These examples are provided to show how photographic data can be integrated with other digitally-captured data and used to study the relationships between the stratigraphic features seen in the photomosaics and the 3D distribution of excavated archaeological piece-plots, geochronological samples, and other kinds of geological samples.

1. Introduction

Archaeological fieldwork has made continual progress in its ability to capture information from the past that is archived in sediments. The different fields of archaeology (complex society, classical, Paleolithic, etc.) though are driven by different questions and these differing questions have pushed fieldworkers to strive to capture different types of information. In Paleolithic fieldwork, a fundamental goal has been to increase the resolution of our data capture so as to refine our understanding of a record that in many cases is produced by hunting and gathering peoples whose economy was such that they left behind very light traces of their activities. Add to this the withering forces of taphonomic processes operating over extraordinary timescales and the Paleolithic archaeologist is typically left with a record that appears frustratingly coarse and maddeningly devoid of information.

* Corresponding author. Tel.: +1 480 965 1077.
E-mail address: erich.fisher@asu.edu (E.C. Fisher).
[1] Co-authors have been listed alphabetically. Co-authorship is shared equally.

http://dx.doi.org/10.1016/j.jas.2015.02.022
0305-4403/

A number of techniques have been developed over the years to tease more diverse and detailed types of information from the sedimentological records at Paleolithic sites. Advances in geochronological, geological, and paleoenvironmental sciences in particular have given Paleolithic archaeologists a much fuller picture of the time and processes involved in the formation of sites (for example, Albert and Marean, 2012; Albert and Weiner, 2001; Bernatchez, 2008; Goldberg and Berna, 2010; Henry et al., 2014; Jacobs et al., 2008; Karkanas et al., 2000, 2007; Madella et al., 2002; Schiegl et al., 2004; Wintle and Murray, 2006; Yoshida et al., 2000). Archaeological deposits must be studied within the context of these sedimentological and stratigraphic frames of reference in order to understand how these records were formed and transformed by various diagenetic processes including geogenic, biogenic, and anthropogenic activities. These changes are often revealed through subtle variations in the color and texture of the sediments seen in stratigraphic sections (Karkanas et al., in press).

The inherently destructive nature of archaeological excavation has also driven the concurrent development of new and better ways to document how a site was dug and what was observed during the excavation process. Traditional surveying devices like total stations have dramatically improved the accuracy of excavation measurements at many Paleolithic sites, allowing for the capture of fine details – like stratigraphic layers or artifact lenses – that would have been otherwise missed with relatively imprecise tape measuring (Dibble et al., 2007; Marean et al., 2010; McPherron, 2005; McPherron et al., 2005). Next generation mapping techniques using close-range photogrammetry and terrestrial laser or structured light scanners are also poised to vastly improve field collection methods of site contexts, including complex geometric surfaces like cave walls (Lerma et al., 2014; Remondino, 2011; Rüther et al., 2009), artifact locations (McPherron et al., 2009), artifact analysis (Shott, 2014; Sumner and Riddle, 2008), and depositional events (Sanger, 2015). An added benefit of these methods is that photographs are often taken during the data collection process using conventional, off-the-shelf digital cameras (De Reu et al., 2013). What these images provide is a visual archive of a site to record features like rock art, which are difficult to map (Chandler et al., 2007; Gonzalez-Aguilera et al., 2009; Lerma et al., 2010), but they can also be used to create photorealistic 3D surfaces of the excavations (De Reu et al., 2014).

Recent developments in digital cameras and lenses have also improved the performance and clarity of images taken under low-light conditions, like in the caves and rock shelters that are common to Paleolithic sites. Post-processing techniques are even able to precisely correct geometric effects, image colors, and merge numerous images into seamless, high-resolution photomosaics that provide unprecedented detail for archival or analytical purposes. These improvements and others, like high definition range photography (Wheatley, 2011), though are being squandered by a persistent underutilization of digital photography within the archaeological sciences. Digital cameras – albeit used frequently and for a variety of purposes – seem to be simply taken for granted or assumed to be good enough if the camera has so many "megapixels" or if the image looks decently exposed (but see, Verhoeven, 2008). There has been no critical discussion, for example, about when it is appropriate to use a Digital Single Lens Reflex (DSLR) camera versus "point-and-shoot", tablet, or phone cameras. Similarly, while the color and quality of photographs taken by many 3D scanners may be good enough to texture those models, these devices are still primarily a scanning tool and secondarily a photographic tool. One must remain critical about the quality and characteristics of these images, such as their lighting or oblique projection from a fixed point, for applications beyond model texturing.

Conventional off-the-shelf digital cameras therefore should not be regarded merely as implements that provide pretty pictures rather than tools that can be used to collect valuable scientific data in their own right. Here, we present the results of a photographic study from the site of Pinnacle Point PP5-6, South Africa to create high-resolution photomosaics of complex stratigraphic sections using a conventional, off-the-shelf DSLR camera. Our study was focused on producing the highest image quality and we discuss what characteristics were important to us in developing this quality, choosing our equipment, and implementing our methodology. We also show how we systematically color-corrected our imagery to create reproducible and meaningful colors for relative colorimetric analyses. In the last section of this paper we describe how we use our photomosaics within an empirical 3D GIS database. We do this 1) to show how photographic data can be integrated with other digitally-captured data and 2) to study the relationships between the stratigraphic features seen in the photomosaics and the 3D distribution of excavated archaeological piece-plots, geochronological samples, and other geological samples.

2. Pinnacle point, Site PP5-6

Site PP5-6 is a rock shelter on the south coast of the Western Cape Province of South Africa, near the city of Mossel Bay. The site is one of a series of coastal caves and rock shelters at Pinnacle Point that has preserved detailed archives of human occupation and climatic and environmental changes spanning the Middle and Late Pleistocene (Bar-Matthews et al., 2010; Brown et al., 2009, 2012; Marean, 2010; Marean et al., 2004; Matthews et al., 2011) (Fig. 1). Sediments have incrementally built up at the base of the cliff in front of PP5-6 since the Last Interglacial high sea stand, ~125,000 years ago, and the preserved sediment stack is now ~30 m tall. Detailed descriptions of these sediments and our excavation methodology can be found in Brown et al. (2012) and Karkanas et al. (In Press).

Excavations into the sediment stack have revealed periods of predominantly Aeolian activity, rock fall, fluvial activity, human occupations, and other natural processes. However, at the base of the stack, a ~5 m tall by ~5 m wide natural truncation of the hillslope has provided the largest continuous stratigraphic section at the site (Supplementary Material). This section is called the "s848 profile" owing to the southing line that the profile intersects perpendicularly. Excavations here have revealed a complex yet unusually detailed sedimentological record due to a high sedimentation rate, which has helped to preserve evidence for repeated, short-term occupations at the site as well as subtle and delicate variations in sedimentological features, like stratified hearth deposits.

Besides excavations, the sheer size of the s848 section impeded its analysis and preservation until recently. Of foremost concern was that continued exposure of the entire section would destabilize the wall and most of the overhead sediments. We therefore wanted to document the s848 section as accurately as possible so that we could continue to study it digitally while conserving the original sediments behind a protective buttress of sand bags. However, the subtle differences in sediment color and very fine changes in the sediment texture, roof spall, and anthropogenic materials posed a unique challenge to the photography. Previous attempts to photograph the section failed because we were unable to control the light sources during the daytime, which created unwanted shadows and altered the colors of the sediments between photos. High Definition Range (HDR) photography was able to remove many of the shadows, but the sediment colors remained unreliable. Moreover, the profile was too large to photograph using a conventional tripod.

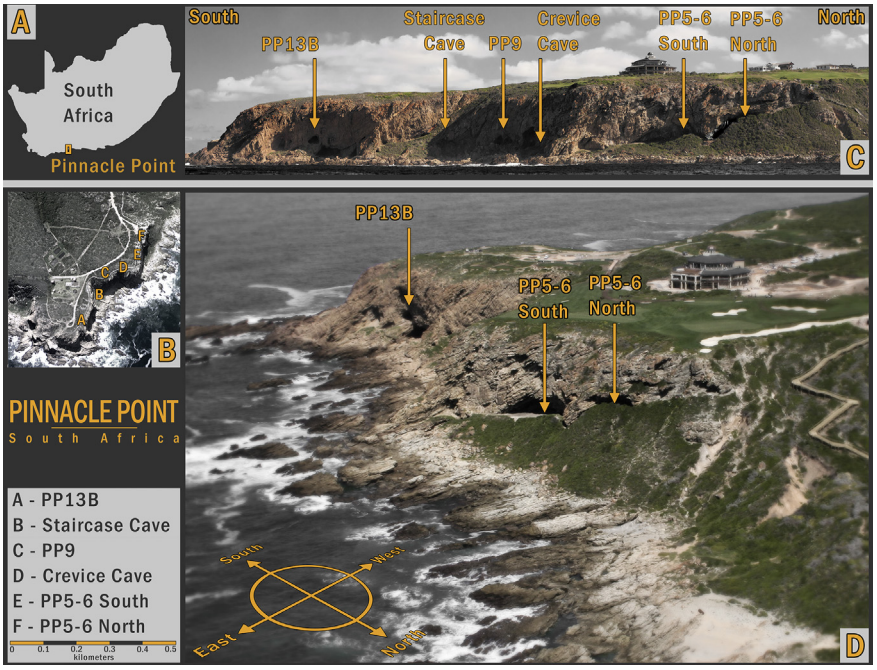

Fig. 1. Caves and rock shelters at Pinnacle Point, South Africa. The location of Pinnacle Point is located in inset (A). Inset (B) provides a top-down layout of the caves at Pinnacle Point. (C) is a panorama taken offshore showing the distribution of the caves within the cliff face. (D) is a low-oblique aerial photograph that provides a good view of PP5-6.

When the camera was positioned far enough away to photograph the entire section then we sacrificed the tiny details in the stratigraphy that made the section so special. Therefore, in 2012 we developed our methodology, which we have described below, to photograph the s848 wall systematically, at night, at close range, and in such a way to record meaningful colors using an objective reference standard. Our photomosaics now provide a useful and unprecedented digital record of the s848 section while the original sediments remain preserved behind sandbags, and we have replicated the method at numerous other large and small sections at PP5-6.

3. Photographic methodology

So many options and opinions are now available that the choice of photographic equipment, and how to use it under varying circumstances, can become a confusing and convoluted process. To simplify our methodology we defined our desired end-result first and then worked backwards to identify the appropriate equipment and the most pragmatic way to apply it in the field. Specifically, we focused our study on producing the highest image quality. This quality was determined primarily by pixel resolution, dynamic range, spatial frequency response, and edge response and secondarily by the image file type. Each of these factors was influenced by the choice of camera and lens, how the data were stored in the camera, and the implementation of the equipment in the field. Fig. 2 provides a workflow for our methodology that corresponds with the following sections below.

3.1. Digital camera

Conventional off-the-shelf digital cameras are affordable and compact tools that are used frequently for documenting archeological sites. These cameras are optimized to capture photographs that appear pleasing to the human eye, but to do so many of these cameras must apply multiple steps of non-linear processing to the recorded images (Akkaynak et al., 2014; Chakrabarti et al., 2009). The reason is due to technical limitations of the imaging sensors and the way that these limitations influence image quality. A digital image sensor is composed of photosites, which measure incoming photons. Larger sensors, like the Active Pixel Sensor (APS) Type-C (APS-C), Type-H (APS-H) or full frame sensors common in DSLR cameras can accommodate bigger photosites so they measure more photons per given time leading to better operation in low-light conditions, using faster exposure rates, all the while producing minimal image noise (Lukac, 2008). Smaller photosites, like those found on many point-and-shoot cameras, tablets, and mobile phones, require either longer exposure times or more signal amplification, which decreases the signal to noise ratio. Smaller photosites also limit dynamic range – the ratio between maximum and minimum light intensities – because they can hold fewer photons than larger photosites so that they are more prone to saturation. Similarly adverse effects are encountered in high megapixel cameras because the photosites have to be shrunk in order to fit more of them onto a sensor. Thus cameras having smaller photosites – typically point-and-shoot, phone, and tablet cameras – provide heavily processed images to counteract the negative effects of their decreased dynamic range. These non-linear modifications, whose details are often proprietary and therefore not transparent to the end-users, alter the linear relationship between scene radiance and the image recorded on the camera sensor. Ultimately, the images that are created may be decent looking, but their processing makes them largely incompatible with scientific methodologies requiring reproducible results or for archival applications where integrity is paramount.

Due to the technical limitations of smaller sensors and photosites archival or detailed analytical applications are best accommodated by APS-C, APS-H, or full frame sensors, which are currently the largest available imaging sensors in commercial off-the-shelf DSLR cameras. In our study we used a Nikon D300s

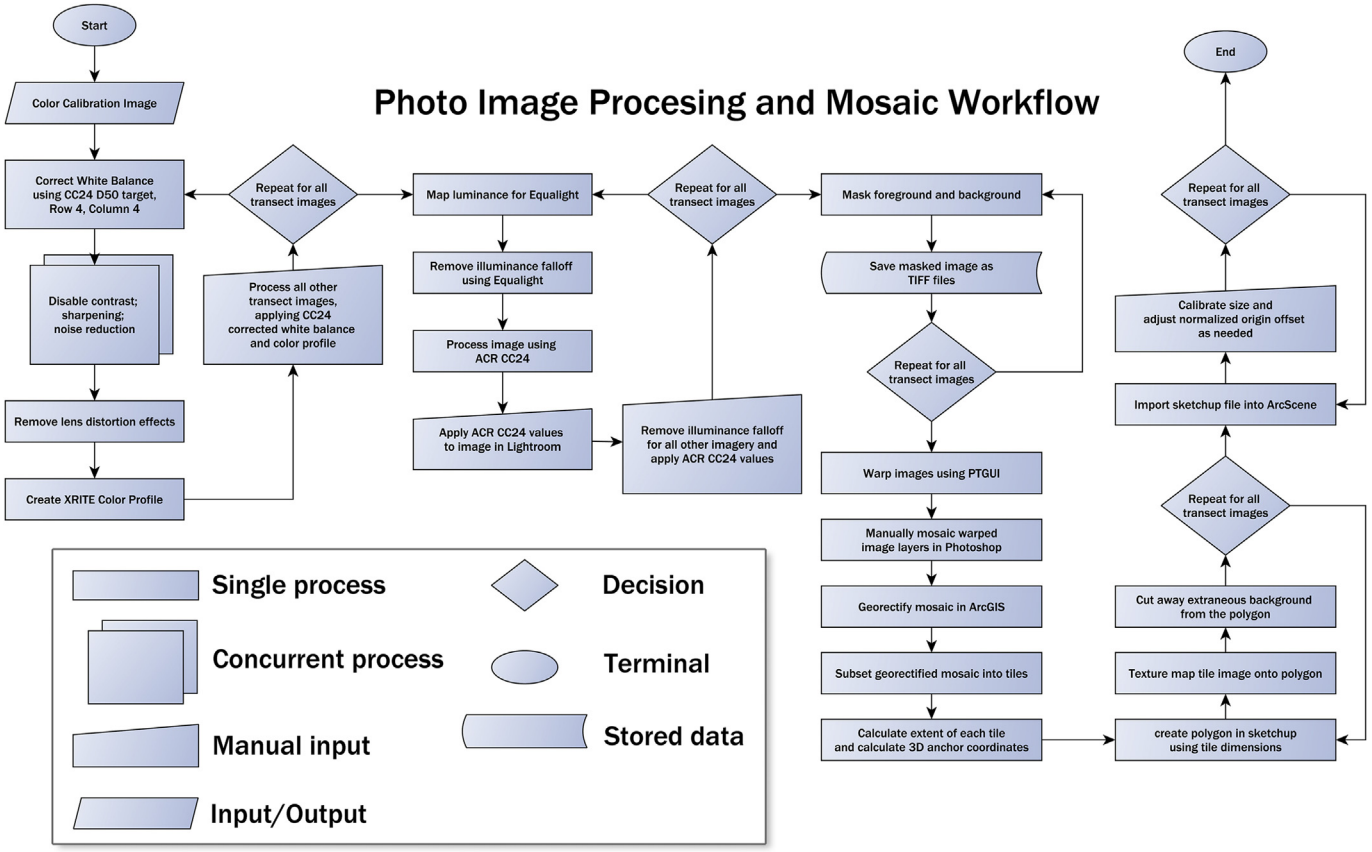

Fig. 2. Flowchart showing the steps used to process the imagery, create the photomosaics, and then integrate these data into ESRI ArcScene.

digital single-lens reflex (DSLR) camera, which uses the Nikon DX APS-C sensor (Nikon, 2009). The size of the APS-C sensor and photosites is outperformed only by the digital full frame reference format (FX), which is 1.52× and 2.4× larger, respectively, than DX.

3.2. Camera lens

Lenses direct incoming light onto the imaging sensor through a series of convex, concave, and aspherical elements. Different combinations of lens element shapes and refractive indexes can be used to alter the image magnification or decrease spherical aberrations, like barrel or pincushion distortion and chromatic aberrations where different colors of light fail to converge onto the same spot. An artificial iris inside of the lens, which is known as the aperture, is also used to limit incoming light as well as change the focal depth.

The two most common lens types are fixed focal length (i.e. 'prime') and telephoto (i.e. 'zoom'). Telephoto lenses allow the photographer to change the image magnification without moving the camera, but they often suffer from noticeable barrel distortion at wide angles and pincushion distortion and increased chromatic aberration when zoomed. Prime lenses are fixed so they require fewer lens elements than telephoto lenses. This makes them lighter and able to let more light reach the camera sensor – which is useful in low-light conditions – as well as take pictures with finer image details. Prime lenses also suffer from chromatic and spherical aberrations, but much less so than telephoto lenses. In our study, we chose to use the AF-S DX Nikon Nikkor 35 mm f/1.8G prime lens. Under low-light conditions it could provide sharp image details and minimal aberrations while shooting at a relatively fast shutter speed that minimizes any blurriness caused by camera movement.

3.2.1. Influence of aperture, depth of field, and focal distance on image details

Lens performance at a given aperture can be measured using the Modulation Transfer Function (MTF), which measures the Spatial Frequency Response (SFR) of contrasting black and white lines within ISO2233 charts (Burns, 2000; Williams and Burns, 2007). Contrast decreases conversely to frequency so a higher SFR means that finer line pairs, hence detail, can be discerned. MTF50 refers to the measured SFR at 50% contrast, which generally accords with a person's perception of image sharpness.

Published MTF50 test results at www.dpreview.com showed that our lens model had the highest SFR at aperture f/3.5 when paired with a Nikon D300 (~1900 line widths/picture height (lw/ph) within the middle 1/3 of the picture frame) (A. Westlake, per. Comm.). Wide apertures like f/3.5 often have the highest SFR, but they also suffer from a much smaller depth of field compared to narrower apertures. Depth of field is the distance between the nearest and furthest objects within an image that appear in focus. Irregular surfaces require a larger depth of field to prevent blurring in areas of high or low relief. In addition to the aperture, the depth of field is also dependent upon the focal distance, which is the length from the focal point of the scene to the image sensor that is denoted by the plane mark on the camera body.

To calculate the focal distance one must account for the camera sensor size, lens angle of view, and the size of the desired area that is captured within an image. Many archaeological excavations rely on a 1 m grid and we have found that it is easier to design

photomosaics and organize the photography if the images accommodate this 1 m grid spacing. Using our camera sensor and lens parameters, we therefore calculated that a focal distance of 1.5 m would cover an area approximately 1.0 m wide × 0.67 m tall, which accommodates the 1 m grid spacing.

A further consideration we had to make concerned the sample frequency of images used to create the photomosaics. In general, a minimum of 1/3 overlap is needed between all adjacent photomosaic images to reduce parallactic distortion (Jacobs, 2004). This overlap also ensures that the center 1/3 of each image is retained where the spatial frequency response is highest while removing the image peripheries that have increased spherical and chromatic aberrations. With 1/3 overlap, four images were required to cover a vertical 1 m^2 area at a focal distance of 1.5 m using our camera and lens.

However, given a focal distance of 1.5 m, an aperture of f/3.6 would only have a 26 cm wide depth of field, which we considered to be too narrow to accommodate irregularities in some of our unexcavated stratigraphic profiles. In contrast, an aperture of f/8 provided a 60 cm wide depth of field. Published MTF50 results showed that our lens and camera models performed highly at f/8 with over 1500 line lw/ph and red/cyan fringing below 0.05% within the middle 1/3 of the picture frame (A. Westlake, per. Comm.). We also calculated our own MTF50 test results using Imatest 3.10 with our equipment set to aperture f/8 and a focal distance of 1.5 m. We sampled four locations on our test photographs of an ISO2233 chart to calculate a mean MTF50 value of 1383 lw/ph (standard deviation (s.d.) = 53.30 lw/ph).

We then calculated the edge rise distance of our images at f/8 and a focal distance of 1.5 m to determine the effective resolution of our photographs. Edge rise distance is a measure of edge blurriness between 10% and 90% pixel values as measured in pixel distances. The mean edge rise in our test photographs was calculated at 2.14 pixels (s.d. = 0.07). We measured 4 pixels/mm in both horizontal and vertical axes of the test images, which was used to convert the rise distance to a metric edge sharpness resolution of 0.54 mm. The smallest observable features in an image should be minimally twice as large as the spatial pixel resolution (Jensen, 2005). Therefore, we calculated ~1 mm effective resolution of our imagery at a focal distance of 1.5 m and aperture f/8.

3.3. Image file type

The file types used by many conventional off-the-shelf digital cameras also impacts quality. One of the most popular file formats is JPEG (Joint Photographic Experts Group), which can provide small file sizes while maintaining relatively high image resolution. Yet the JPEG format is lossy, which means that pixel information is lost when the image is compressed. JPEG image quality is also cumulative and repetitively altering and saving a JPEG image progressively decreases the image quality (Pennebaker and Mitchell, 1993). TIFF files (Tagged Image File Format) are another common file format that can use either lossy compression or lossless techniques, which do not alter the image quality. However, the image properties of TIFF files are still altered using the camera's internal settings, which means that the image results may not be reproducible (Adobe Developers Association, 1992). In contrast, camera RAW file formats, like Nikon *.NEF, Canon *.CR2, or Adobe *.DNG, preserve the original data registered by the image sensor and encoded any post-processing changes into a separate file. This allows the original data that was registered by the image sensor to be manipulated and preserved if different modifications to the image need to be made. The downside to RAW files though is that the preservation of the full array of digital data creates significantly larger files than either JPEG, TIFF, or many other file formats. In our study we collected all of our imagery using the Nikon RAW (*.NEF) 16-bit format, which preserved the most amount of data collected by the imaging sensor in the stored file.

3.4. Scene lighting

We used twin Nikon speedlights (SB80DX and SB800) to illuminate each scene. The Nikon speedlights were set to Manual mode (to ensure a consistent output flash intensity), ISO 200, f/8, and zoom head position at 24 mm (widest flash dispersion). The flash sync speed was set to 1/250″ to minimize the influence of ambient light on the image white balance and color, but all imagery were shot in total darkness anyway, which effectively prevented ambient light interference. The flash intensity was adjusted using test images where the capacitor output was adjusted in 1/8 increments from 1/128 to 1/1 (full discharge). Each test image was checked for dynamic range clipping using Adobe Lightroom. Minimal clipping was observed at 1/8 and subsequent fine-tuning in 1/3 steps removed all visible clipping from the test images. The final speedlight capacitor settings for pitch black conditions and a focal distance of 1.5 m were: SB80DX: 1/8 (−0.3) and SB800: 1/8 (−1/3).

We anticipated an irregular illumination pattern in our images because we used two speedlights. The spatial distribution of light intensity in an image varies relative to the fourth power of the cosine of the angle of incoming light on a camera sensor array (Gardner, 1947). This variation is called the *illumination falloff law* and results in a darkening along the periphery of the image outwards from the center. It is one type of vignetting that results in an inconsistent light pattern across images, which makes seamless photomosaic imagery difficult to create, if not impossible. Functions like Adobe Lightroom's Lens Correction Vignetting Tool can remove cosine-fourth illumination falloff effects, but only if the light distribution follows a single-point, radial pattern. We therefore mapped the irregular flash illuminance pattern created by photographing a solid white background with the predetermined flash intensity settings at 1.5 m. A 16-bit copy of this image in *.TIFF format was then imported into Equalight 3.0, which was used to correct illuminance on a pixel-by-pixel basis within each image. Prior to this operation, we used Adobe Lightroom to set each image's contrast to linear, which maintained linearity to the scene radiance. Sharpening and noise-reduction were also disabled to minimize acutance influences.

4. Color calibration

Color spaces are organizations of colors that can be related to mathematical values or other classification systems using color models. Many color spaces used today are based on CIE 1931 (Commission Internationale de l'Eclairage), which is a mapping of color based on standard human perception (CIE, 1932). This includes the tristimulus CIE XYZ and the CIE RGB color spaces as well as the color-opponent L*a*b* color space.

All image sensors, display devices, and printers handle colors slightly differently so a transformation is required to convert these device-dependent colors to a standardized, device-independent color space before meaningful quantitative colorimetric comparisons can be made (Akkaynak et al., 2014). One of the most common device-independent color models is CIE L*a*b* because it is based on the human perception of color and not on the physical properties of a device. This model uses an ultra-wide gamut to mathematically model colors using three channels: L* (lightness), a* (red−green chrominance), and b* (yellow−blue chrominance). We used an XRITE ColorChecker Passport to transform our device-dependent image colors to the device-independent CIE L*a*b* color model. The ColorChecker Passport contains 24 color targets and

the L*a*b* values for each target are published by X-Rite (2012) using the CIE D_{50} illuminant, which is a representation of clear sky daylight conditions at noon (5003 K). The D_{50} illuminant is also the ISO 3664:2009 international standard for graphic arts and photography (ISO, 2009) and it is based on a similar light temperature to our Nikon speedlights (~5500 K), which benefits the accuracy of our color calibrations. We performed the color calibrations using the Adobe Camera Raw Calibrator CC24 Version 8, which was developed by Rags Gardener (http://www.rags-int-inc.com). This plugin to Adobe Photoshop matched the measured L*a*b* values of each ColorChecker patch in our images to its published equivalent by adjusting the Camera Raw value for temperature, contrast, and brightness values as well as red, green, and blue hue and saturation.

4.1. Color calibration comparison

We used the CIE ΔE_{2000} metric to quantify differences between our measurements of the calibrated colors in the images and their published colorimetric values. ΔE_{2000} weights L*a*b* values to compensate for the way that human vision differentiates color variations in different parts of the visible light spectrum (Luo et al., 2001). A ΔE_{2000} value of 1 indicates a just noticeable difference; meaning that the two solid colors under comparison are not discriminable to the eye.

The mean ΔE_{2000} of all ColorChecker patches from all transects was 2.56 (s.d. = 1.42). This low value suggests that there are only minor perceived differences between the calibrated color measurements and their published colorimetric values, which may or may not be discriminable to the human eye (see Fig. 3 for visualizations of these differences). In particular, common colors in our images and stratigraphy (red, orange, orange-yellow, and yellow) had a mean ΔE_{2000} of 1.66 with a similarly low standard deviation of 0.88. These results show that there was relatively little variability in these colors across all of the images and that the colors accord closely to their published standards, as can be seen visually in Fig. 3.

5. Photomosaics

The images were prepped for the photomosaic process after we completed the color calibrations. This process included removing areas in the images were parallactic effects and blurriness were most pronounced, typically in the foreground and background because the focal range was centered onto the image midground. We masked these unwanted areas in our images using monochromatic green, which is a color that does not occur naturally in our study sites and therefore stands out and can be easily identified by image processing programs. The masked images were then exported as 16-bit *.TIFF images in the wide gamut ProPhoto color space, which maintained the image color fidelity, and then imported into PTGui v9.1.8 (www.ptgui.com). PTGui looks for pixel-based similarities across overlapping images to establish tie-points that are ultimately used to warp the images into a single photomosaic using one of several predefined projections. We refined the automatically generated control points manually by adding new control points that linked key features visible across images, like our photo rectification chits, which are described in Section 6.1 below. Table 1 shows the photomosaic results; the mean and standard deviation of the control point errors in all of our photomosaics was below 1 cm.

The original color fidelity and resolution were also maintained in the exported photomosaic files. To do this, we exported the individual warped images within each mosaic as separate layers of an Adobe Photoshop Large File (*.psb), which can accommodate images up to 300,000 × 300,000 pixels in size. Each photomosaic file was imported into Adobe Photoshop where the overlapping images layers were checked for lingering parallactic effects. Distorted or non-aligning areas were removed manually. Monochrome green areas were also removed at this time. We then used the Auto-Blend function in Adobe Photoshop to create the mosaic image masks, which masked non-relevant sections of each layer to create a single continuous photomosaic. The image masks were checked individually before the layers were merged. The final photomosaic was saved as a 16-bit Photoshop file in the ProPhoto RGB color space. The photomosaic was also converted to the sRGB IEC61966-2.1 color space and saved as a separate TIFF file because ESRI ArcGIS currently cannot render wide gamut color spaces.

6. Integration of the photomosaics within our GIS

The finished photomosaics in the ProPhoto RGB color space provide the most reliable colors and highest resolution. These images are ideal for referential and archival purposes, especially if they are going to be viewed in programs that can accommodate wide-gamut color spaces like Adobe Photoshop. Otherwise, the images are largely unsuitable for more detailed analytical purposes because they lack a reference system. Projecting an undefined image into a 2D coordinate system is known as georectification, a process that uses tie points within an image to shift, scale, rotate, and stretch a raster image into a geographic space. Once an image was georectified then features within the images can be measured, new features can be overlaid, and correlations can be made to other datasets.

Current georectification methods though are largely 2D-based, which prohibits detailed comparisons between the photomosaics and features with highly variable spatial distributions and morphology, like stratigraphy. To complicate matters further, the popular ArcGIS software suite currently cannot render vertical raster images, so even if one could 3D georectify an image then it still could not be displayed in their 3D programs. ArcGIS is the industry standard software for GIS processing and analysis and it is also the platform that we used to develop our geodatabases, which can be accessed by our colleagues worldwide. Therefore, we developed a workaround that uses image texture mapping onto 3D vector models to display our georectified photomosaics in ArcGIS 3D applications. This simple solution offers us a more robust and intuitive way to observe sedimentological changes seen within the images against other archaeological spatial phenomena.

6.1. 2D georectification

The stratigraphic sections were tagged with 1 cm^2 target chits in a 20 cm grid pattern, which were shot in with a total station. These chits served as references for the georectification and we used ESRI ArcMap 10.2 to georectify our 16-bit sRGB photomosaics into the South Africa National Grid, Lo. 23 (Hartebeesthoek94 Datum). Chit coordinates on southerly facing profiles were transformed to a planimetric perspective by assigning the measured easting values to the X-axis and the measured elevation values to the Y-axis. Alternatively, the northing values on east or west-facing sections were assigned to the X-axis while elevation values were still assigned to the Y-axis (Bernatchez and Marean, 2011). These chit locations were then matched to their measured point locations in ArcGIS. We were able to use a spline transformation to reduce the residual errors between the imaged and measured chit locations because of the density of reference points and the standardized ~20-cm gridded chit spacing. For each photomosaic, the final warp showed imperceptible offsets at the chit locations and no visible rectification errors in-between the chits.

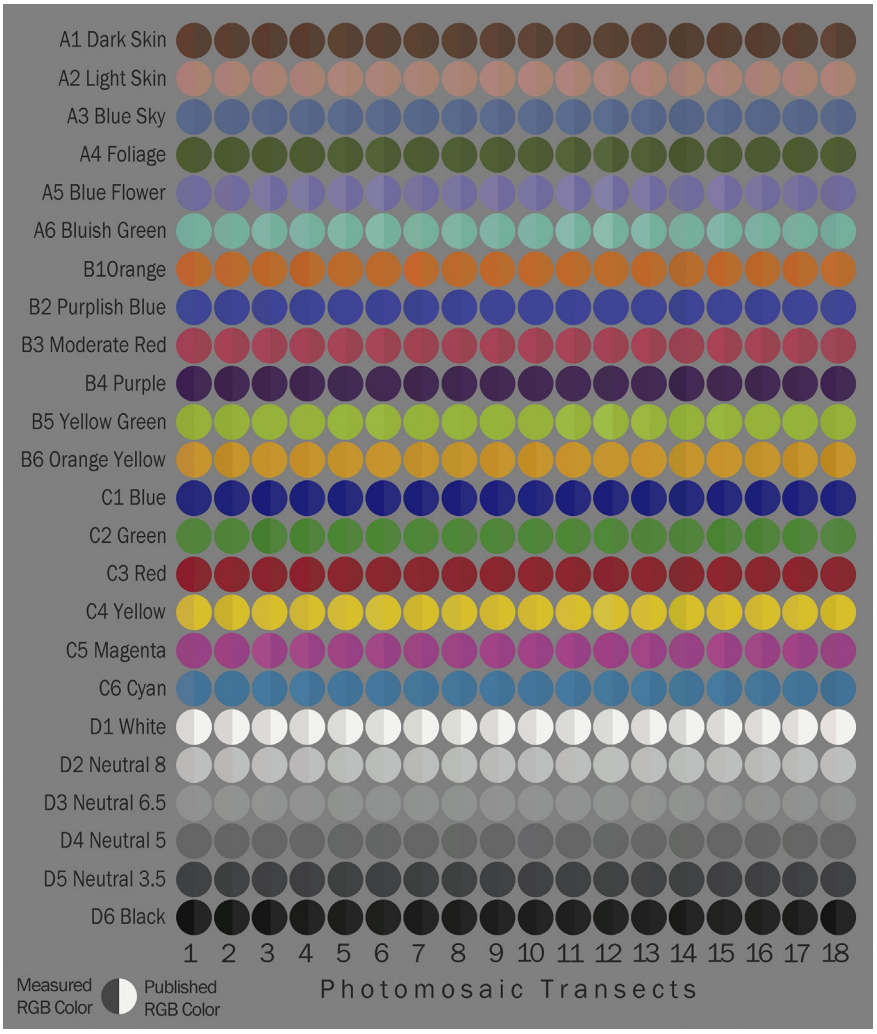

Fig. 3. A side-by-side comparison of the ACR CC24 calibrated color targets from each transect (left circle half) and the published colorimetric data from XRITE using the D_{50} illuminant (right circle half). The colors are presented within the sRGB color space. The chart can be used to visually determine the accuracy of the color calibrations. (For interpretation of the references to color in this figure legend, the reader is referred to the web version of this article.)

6.2. Texture mapping

Texture mapping aligns a digital image with a 3D model so that the image can be mapped to its surface. The images are mapped to the U-V axes of 3D models, which are based on the width and height of the image. In this way rectilinear images are easier to position precisely than irregularly-shaped images.

We exported the images from ArcMap as 8-bit TIFF images in order to auto-generate their rectilinear bounding boxes. We simultaneously used this process to subset large images into tiles <45 MB so that they would render correctly in Trimble Sketchup, which we used for the texture mapping. After being exported, the horizontal and vertical extents of each tile were then calculated using South Africa National Grid coordinates. These data were used to calculate the 3D coordinate of the lower right corner of each image tile, which would be used to anchor the sketchup files in ESRI ArcScene. For north or south-facing profiles, the Northing coordinate was calculated as the mean of all photo chit Northing values while the Easting value was taken from the right image extent. Height was taken from the bottom extent of the image. Alternatively, a similar protocol was used for east and west-facing profiles except that the calculated Northing coordinate of the anchor was derived from the mean of the Easting photo chit coordinates.

2.5D polygons corresponding to each tile extent were then drawn individually using Trimble Sketchup 2013 and the images were textured in turn onto the respective polygon front face. The image bounding box that was created by ArcMap was also cut away, leaving only the original, irregular image border. Several pixels were left in the lower right corner or the upper left corner to preserve the original dimensions of the tile, which was important for correctly placing and sizing the textured polygons in ArcScene. The textured polygons were finally saved as a Sketchup version 6 file, which was compatible in ArcScene.

Table 1
Results from the photomosaic process, showing that the mean and standard deviation of the control point errors in all of our photomosaics was below 1 cm.

Profile	Number of images	Number of control points	Mean distance, pixels	Standard deviation, pixels	Mean distance, mm	Standard deviation, mm
Left	66	22,331	32.94	27.77	8.24	6.94
Right	73	39,282	30.64	29.90	7.66	7.47
Center 2	15	2,919	12.01	8.48	3.00	2.12
Center 3	14	2,858	9.16	5.51	2.29	1.38

6.3. 3D rendering

The 3D anchor coordinates that were calculated from the lower right corners of each image tile (Section 6.2) were then imported into ArcScene as a single Z-aware (3D) point file. The point symbology was subsequently adjusted to show individual points so that each anchor could be assigned to its respective sketchup file. The imported sketchup models were true to scale because pixels had been retained in each corner of the texture mapped images during the sketchup processing. However, the normalized origin offset (north–south, dx or east–west, dy) had to be adjusted so that the anchor corresponded to the correct corner of the Sketchup model. As a final step, the symbolized point shapefiles were converted to multipatch feature classes and stored in an ESRI File Geodatabase. This procedure was done because file geodatabases store vector datasets in a compressed format that makes it easier to store and render large files.

Our methodology therefore projects 2D-georectified raster imagery from a 3D-point anchor position, sidestepping known limitations for georectifying and rendering vertical raster datasets in ESRI 3D software. The anchor positions the raster image within a real-world three-dimensional coordinate system while georectifying the image in profile allows the actual image dimensions to be mapped into the correct 3D context. This methodology can be used to project positive and negative Z-axis imagery on or off-axis. The profiles can be oriented along any azimuth parallel to the XY-coordinate plane though it is much simpler to render imagery when there is a one-to-one relationship between an axis and image azimuth. Once the profiles are integrated into the 3D databases then they can be studied relative to other vector or raster-based GIS datasets, such as artifact or sample locations or digital elevation models of excavation surfaces. In the next section we provide a brief case study showing how we use our 3D georectified photomosaics to classify archaeological plotted finds and complex stratigraphy at Site PP5-6.

7. Case study: Site PP5-6, South Africa

Using macro- and microscopic forms of analysis, we have been able to classify the s848 section into three distinct groups of strata, which we call “Stratigraphic Aggregates” since they include many other, smaller layers that formed under similar circumstances (Karkanas et al., in press). At the base of the sequence are the Yellow Brown Sands (YBS), which are anthropogenically-sterile dune sands that have a weighted mean Optically Stimulated Luminescence (OSL) age of 96 ± 6 ka (Karkanas et al., in press). The YBS is overlaid by the roofspall-rich Yellow Brown Sands and Roofspall (YBSR), which is itself overlaid by the Light Brown Sand and Roofspall (LBSR). These deposits have weighted mean OSL ages of 89 ± 5 ka and 81 ± 4 ka, respectively (Karkanas et al., in press) (Supplementary Material).

Excavations into LBSR, YBSR, and YBS ended recently and this work has revealed numerous vertically-discrete clusters of plotted finds. The points within each cluster are believed to be topologically related, due either to post-depositional processes or as a generalized reflection of ancient land surfaces on which the points were deposited. Many dense assemblages of points also exhibit their own internal spatial clustering, which may indicate spatial patterns during more intensive occupations of the site. Gaps separating packets of thin point lenses or dense assemblages of plotted finds serve as a way to classify both the clusters and areas in-between into different anthropogenic units, which we call Sub-Aggregates that often correlate to palimpsest anthropogenic events, like shell-rich layers or combustion features.

Until recently, the classifications of Stratigraphic and Sub-Aggregate sediments could only be crudely associated with the distributions of the plotted finds in our GIS databases yet we could clearly see important features in the plotted find points that related to the stratigraphy. This included, for example, clusters of points that were believed to belong to previously unrecognized sub-aggregates or even differences between the points and visible stratigraphy that could be used to refine the definition of our existing classifications. Therefore, after developing our methodology to incorporate vertical imagery into the 3D GIS, we set out to photograph the s848 profile and adjacent east–west facing profiles.

The (~5 m × ~5 m) size of the s848 profile required a custom mobile platform for our camera and flashes that would allow us to systematically map a section from <1 m to >5 m tall while maintaining a constant horizontal and vertical image overlap and focal distance (Fig. 4). The platform was built out of aluminum to prevent corrosion in marine environments. It consisted of a base plate, a single 5 m mast, and an adjustable boom. The base plate was also constructed using adjustable rubber feet to accommodate irregular surfaces. The mast was subdivided into five 1-m long sections, each having a 20-cm long reducer coupling on one end to slot the segments into one-another. 1 cm diameter holes were drilled through the mast segments every 5 cm. These holes were used to align each of the mast sections and to position the boom vertically. At the top of the mast was a cap with four cables that were affixed to bolts in the rock shelter walls. Turnkeys allowed each of the cables to be tightened independently, which secured and leveled the entire camera frame.

The boom consisted of a single horizontal rib that was affixed to the mast via a sleeve and it supported a 50 × 20 cm face plate. A camera tripod ball-head was attached to the face plate 30 cm from the mast. Sliding L-brackets were attached to the centerline of the face plate 15 cm on either side of the tripod head. These L-brackets were used to attach twin Nikon speedlights, and their position could be adjusted horizontally and vertically. Flash diffusion paper was placed in removable 20 cm × 20 cm panes in front of each Nikon speedlight. Each speedlight was positioned approximately 3 cm behind the flash diffusion paper and aligned forward with the LCD screen facing up. The speedlights were connected to a Nikon D300s using PC sync cords that connected to a hot shoe adapter with twin PC female outlets. The boom was designed to be fully reversible so that two vertical transects could be shot around the mast from a single setup. Four vertical transects could be shot when the boom was lengthened using a detachable extension that positioned the camera and speedlights 73 cm from mast.

Over a period of 5 nights, we used the setup described above to collect over 400 photographs that were eventually processed into 18 individual profiles, each having an effective pixel resolution of 1 mm (Section 3.2.1.). When integrated into our 3D GIS database, we were able to trace thin clusters and dense assemblages of plotted finds, representing shell-rich lenses, combustion features, and stratigraphic boundaries among other things, across the excavations and link these layers unambiguously to different sedimentological features visible within the profiles regardless of the strike or dip of the strata (Fig. 5). The stratigraphy could thus be mapped over the entire excavation area.

Furthermore, we were able to apply our methodology to integrate photographs of micromorphological samples so that we could tie in the microstratigraphic context, which has been shown to provide key information about the depositional and life history of archaeological sites (Goldberg and Berna, 2010; Karkanas and Goldberg, 2010). In fact, we were able to apply a multi-scalar approach to integrate the micromorphology samples into our models (Supp. Online Movie). To do this, we recreated the original sample dimensions in 3D using points taken before the sample was

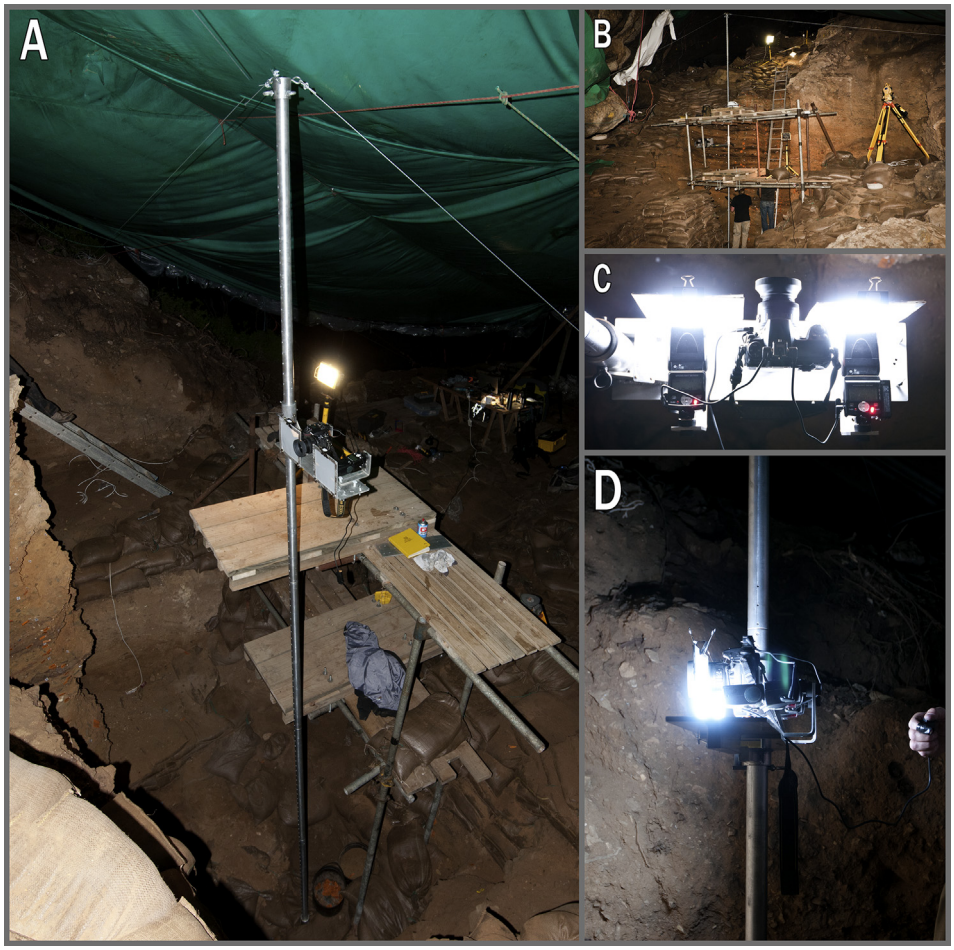

Fig. 4. Multiple views of the camera platform and mast set up in front of the south 848 profile. (A) Oblique view looking down at the 5 m high mast and camera platform. Note the guidewires and that the camera is in shooting position. (B) Looking north at the scaffolding and camera frame in front of the south 848 profile. (C) Top-down view of the D300s and Nikon speedlights on the camera platform. Note the flash diffusion paper and that the image was taken in pitch black conditions. (D) Profile of the D300s and Nikon speedlights on the camera platform.

removed from the section (Fig. 6A). Photographs of the resinated micromorphology samples were then georectified and integrated into our 3D model, which provided a meso-scale level of analysis. Fig. 6B, for example, shows how the georectified photograph of resonated sample #110601 articulates with the spatial distributions of 3D plotted finds and other section imagery.

Supplementary video related to this article can be found at http://dx.doi.org/10.1016/j.jas.2015.02.022.

Moreover, sample #110601 is located at the top of the s848 profile, and sand and roofspall-rich (SR) deposits (Kyle SR and Adrian SR) separate shell-rich and ash deposits (Katherine Shell, Kyle Shell, and Adrian Shell). Closer observation shows that the 3D points can be classified into charcoal and ash-rich layers using the observed sediment descriptions during the excavations (Fig. 6C). Upon closer observation, the distribution of these layers lines up with the microstratigraphic visible in the resonated slab (Fig. 6D). Integrating photographs of the thin-section slides subsequently allowed us to study these features at a micro-scale level of analysis, showing a more nuanced distribution of burnt bone, shell, ash, and charcoal in this sub-aggregate (Katherine Shell), complete with the characteristic banded structure of *in situ* hearth deposits and a clear layer of cemented ash (Fig. 7).

Combustion features seen within the section imagery can also be associated to other proxies for burning, like magnetic susceptibility. For example, the Cobus Shell is a 15 cm thick, shell-rich lens of >950 plotted finds that are separated into two diffuse lenses. Between these lenses is a layer of fewer plotted finds and charcoal-rich sediments that is visible in the profiles overlaying rubified, shell-rich sands. Like the Katherine Shells, the dip of the Cobus Shell strata makes it difficult to associate its plotted finds directly to the features seen in the sections without using 3D. The same is true of the magnetic susceptibility (MS) analyses of bulk sediment samples. Yet when these data are shown with the plotted finds and sections in 3D one can clearly associate the much higher MS measurements (mean = 327.0 10^{-8} m^3 kg^{-1}; s.d. = 6.99; n = 2) to the charcoal-rich layer and the lower MS measurements to the surrounding sediments (mean = 40.8 10^{-8} m^3 kg^{-1}; s.d. = 13.35; n = 7) (Fig. 8 and Supp Online Movie).

Like other mineral magnetic parameters, MS has been proven to be an excellent proxy for identifying burnt materials (Herries, 2006, 2009, 2014; Peters et al., 2000, Peters et al., 2002). Previous studies at Pinnacle Point have shown that the 3D spatial distribution of *in situ* or redistributed hearth remains typically have higher MS measurements than unburnt sediments (Herries and Fisher, 2010). Thus while the MS and plotted find data may reveal anthropogenic influences on the natural environment, in this case burning or waste disposal, their integration with the photomosaics in 3D gives these data context. The large disparity between the number of plotted finds from within the charcoal-rich layer (n = 170) and those found in the surrounding sediments (n = 797) may also

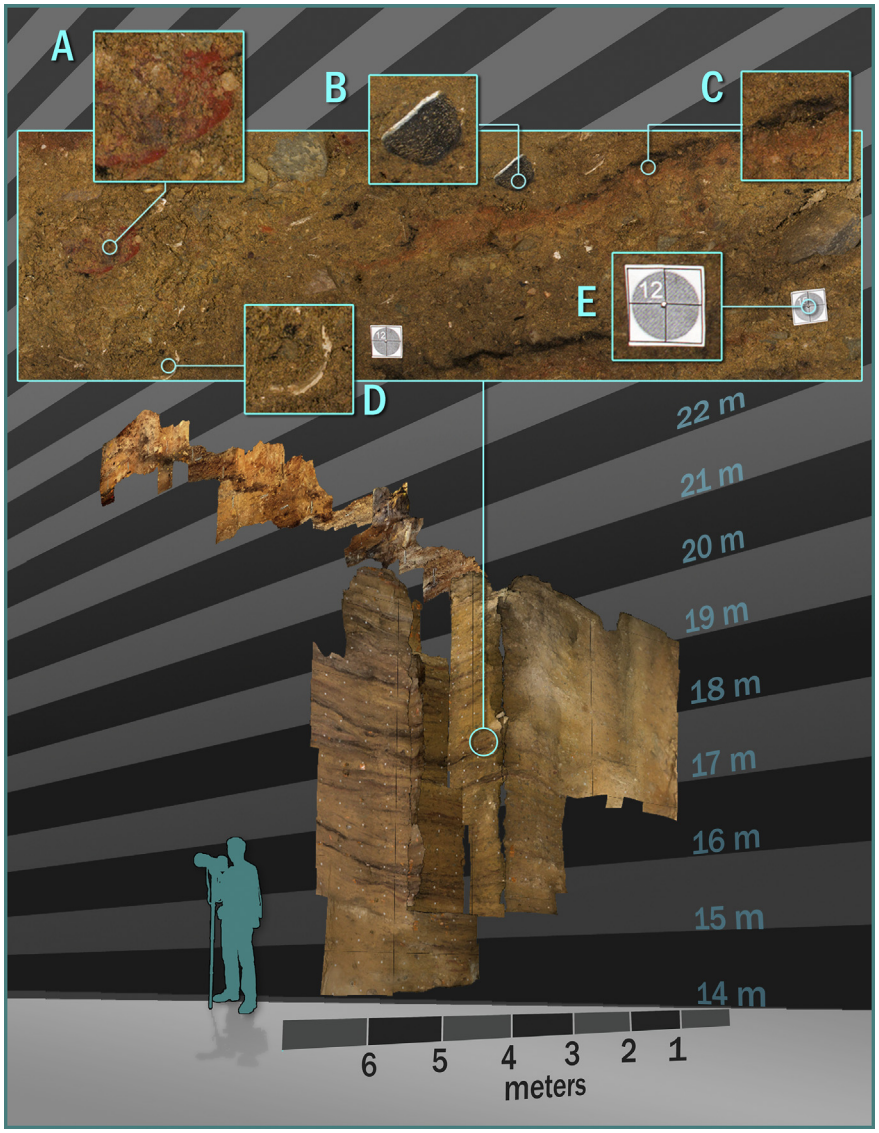

Fig. 5. Composite image of the s848 profile and associated long section profiles looking obliquely to the northeast. A silhouette of a 6 ft (1.83 m) tall person has been superimposed for scale. A portion of the west 727 profile is enlarged above, showing the level of detail that is available in the imagery: (A) pigment nodule; (B) burnt bone; (C) charcoal and rubified lenses; (D) marine shell; (E) 1 cm^2 chit. Note that the crosshair lines on the chit are 1 mm wide.

reflect past human behavior at PP5-6. Following ethnographic studies on modern hunter–gatherer use of hearths (Binford, 1980), one might infer from our 3D GIS model that the hearths like the Cobus Shell were not used to discard waste at PP5-6.

In addition to the micromorphology, magnetic susceptibility, and other samples we have taken across the site, one can also easily work through the geochronology of the sequence within the 3D GIS. Seventy-six sediment samples have been collected and dated for optically stimulated luminescence from the entire PP5-6 sequence (Brown et al., 2012). These samples are integrated into the GIS model as 3D cylinders matching the size and diameter of the plastic tubing that were pushed into the profiles to collect the sediment samples. The modeled age and one standard deviation are represented at the end of the tubes using 3D text (Fig. 9A).

We use the GIS and photomosaics to provide contextual information for our OSL samples. In many cases we excavate squares before we sample for OSL, so we are able to re-create the context using the GIS and photomosaics. This allows us to macroscopically observe any factors that may arise from the placement of the samples that would directly influence the equivalent dose and dose rate estimates, which are the numerator and denominator in the OSL age equation. We can also model the context of OSL samples after the fact to observe if we accidentally have cross-cut two stratigraphic aggregates of different ages or have penetrated with the sample tube any truncation fill or modern overburden, for example.

Furthermore, we can also use the photomosaics and 3D GIS to obtain valuable information that aid our understanding of the radiation dose to which the samples have been exposed over their burial history. It is the omnipresent ionizing radiation in the form of alpha- and beta-particles and gamma- and cosmic-rays that is responsible for the movement of electrons into traps in the crystal lattice of mineral grains, such as quartz and feldspars, and that fill these traps at a constant rate through time (Aitken, 1985; Jacobs and Roberts, 2007). Each radiation type has a different sphere of influence ranging from a few microns (alpha-particles) to a few tens of meters (cosmic-rays). Fig. 9B shows an example for one of our samples where the beta (2–3 mm radius) and gamma

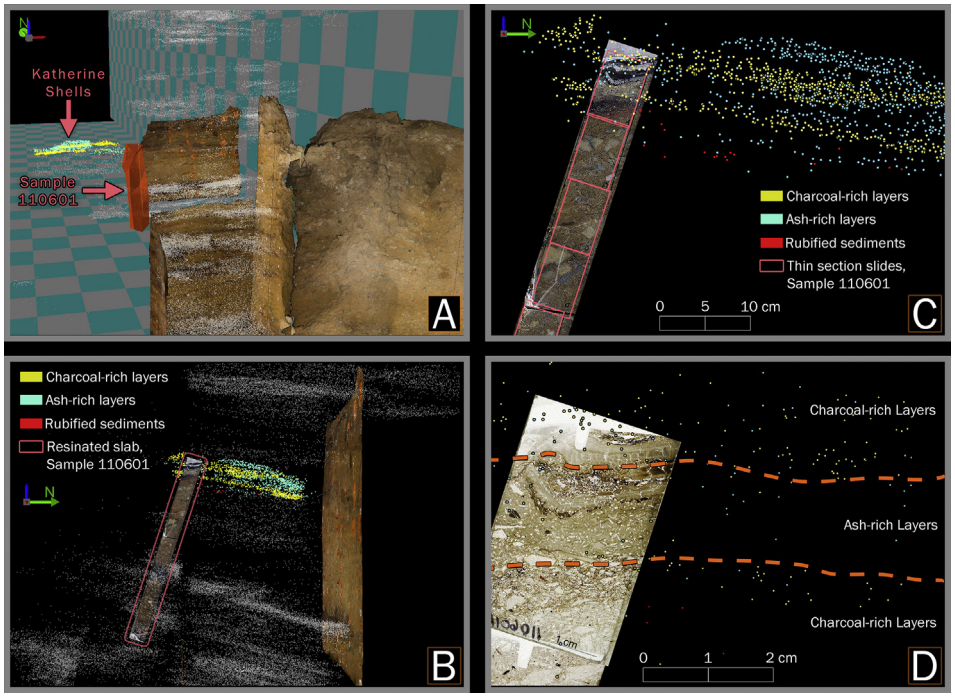

Fig. 6. Composite image showing how the methodology described in the paper can be applied to micromorphology samples for detailed 3D analysis. (A) View looking NW at the section images with the shape of micromorphology sample #110601 represented as a 3D polygon. (B) Georectified image of the resonated slab from sample 110601 integrated into the 3D GIS. Plotted finds are represented as white points except in the Katherine Shell sub-aggregate where the points are color-coded by their sedimentological context. (C) Close-up of the resonated slab with each thin section slide location outlined in pink. Note that the combustion feature banding in the resonated slab closely aligns to the sedimentological context of the plotted finds. (D) Close up of thin section slide A showing the close articulation between the major micro-stratigraphic changes and the 3D plotted finds. (For interpretation of the references to color in this figure legend, the reader is referred to the web version of this article.)

(~30–40 cm radius) spheres of influence span two sub-aggregates in the LBSR. It is clear that the sediment surrounding the samples is not homogeneous, but it is at least now possible to assess the possible influences of the different components on the dose rate in a more informative manner. The cosmic-ray dose rate has a ~30 m sphere of influence and in a rock shelter, such as PP5-6, the angular distribution of the cosmic rays and its penetration and attenuation through rock and sediment of different densities and depths should be accounted for. With the GIS, we are also able to reconstruct the present situation with accuracy and precision. Fig. 9C shows a diagrammatic example of our model for estimating this parameter. We can, therefore, now use the GIS to observe the 3D context of each sample location and more accurately model the sphere of influence for each radiation type and any disturbances or inaccurate sampling. This gives us more information about the radioactive context of the sample and the deposition and post-depositional position of our samples, which can be used to refine the precision and accuracy of the modeled OSL ages and errors.

8. Discussion

We designed our photographic methodology so that it could be applied to a wide range of situations and collect data relatively quickly without compromising quality or requiring specialized equipment, software, or training. It was for these reasons that we intentionally used commercially-available, off-the-shelf photographic equipment. There are hundreds, if not thousands, of different camera and lens options available that suit a broad spectrum of budgets and applications, ranging from microscopic photography to monumental architecture. In fact, a professional or semi-pro DSLR camera may not even be necessary now. Mirrorless camera systems are becoming quite common and many of these cameras can capture images in RAW formats using the 1.5″ or micro four thirds (17.3 mm × 13 mm) sensors. While these smaller sensors still do not provide the same dynamic range and low-light response of professional DSLR cameras, they may be suitable for a variety of applications. An added advantage is that most mirrorless systems are also significantly lighter and cheaper than DSLRs.

In fact, the primary limitation of our methodology concerned the photography equipment that was used to collect the imagery. We used a Nikon DX camera system in our study because it was readily available and it also suited the technical aspects of our imaging needs. Had we used a Nikon FX camera (or full-frame equivalent by another manufacturer) and 35 mm lens then the field of view per image would have been ~40% larger, allowing us to either move the camera closer to the section (to increase pixel resolution) or to capture a larger area in each photograph (to decrease the number of images required for each photomosaic). A single photograph therefore could be collected for a 1 m × 1 m profile using a full-frame system and our setup. In comparison, a micro four thirds camera would have collected images that were between ~40% and ~67% smaller than equivalent DX and FX images, respectively.

The software that we used was also entirely commercially available, and save for ESRI ArcGIS and Adobe Photoshop, it was either relatively inexpensive or free for non-commercial activities (e.g. Trimble Sketchup and Adobe Camera Raw Color Calibrator). This includes a new MATLAB (Mathworks, Inc., Natick MA) color calibration protocol that we are beginning to apply, which was described in Akkaynak et al. (2014) and provides improved color calibration results. The methodology was developed specifically for scientific data acquisition using consumer cameras to ensure accurate and consistent color capture every time. Each step of this workflow is also mathematically quantified, giving users control over each processing step. The script is available for download

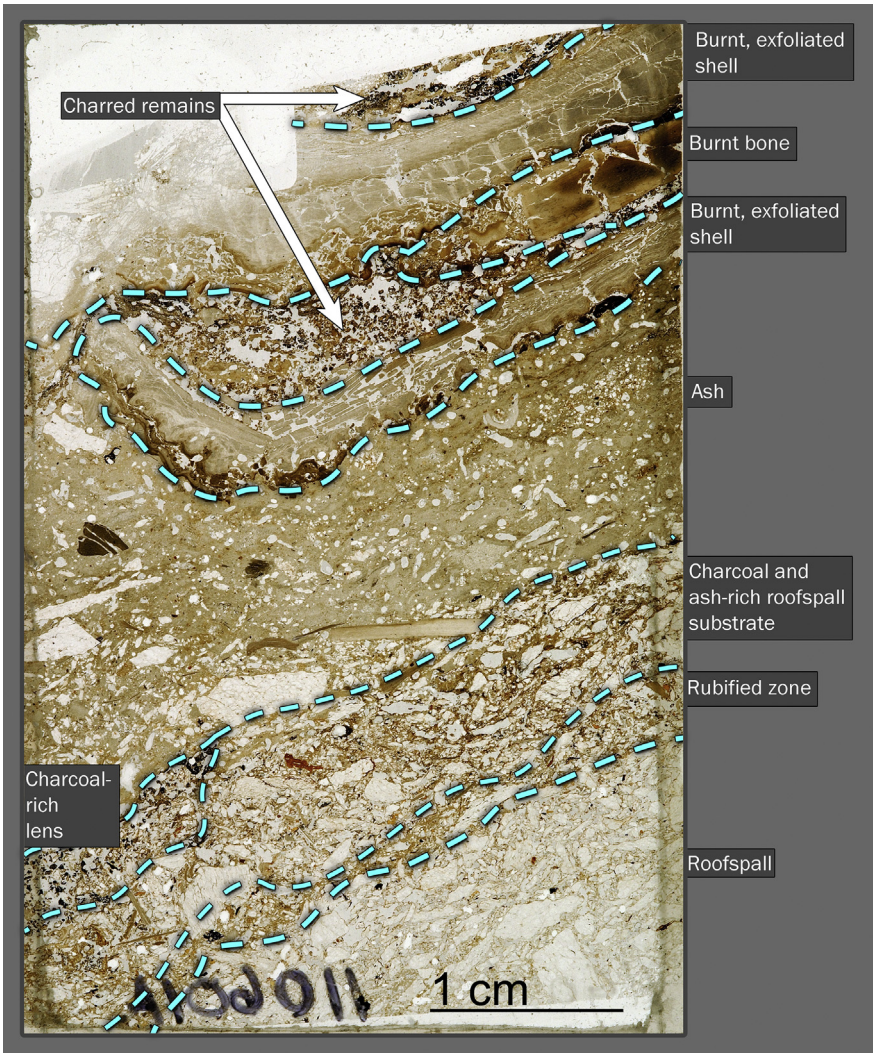

Fig. 7. Thin section slide A from micromorphology sample 110601. This sample shows stratified layers of burnt remains and cemented ash overlaying rubified sediments and roofspall-rich sediments.

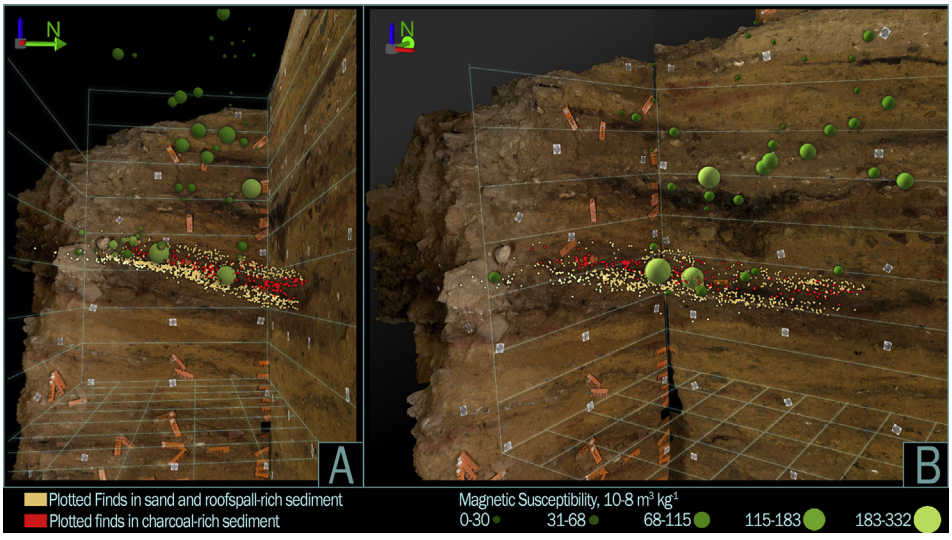

Fig. 8. Composite image showing two views of the plotted finds and magnetic susceptibility (MS) samples in the Cobus Shell sub-aggregate. The plotted finds have been color coded based on their sedimentological context. The MS values are greater within the charcoal-rich sediment context, which can also be traced clearly back to the combustion feature seen in the south-facing and east-facing sections despite the sloping deposits.

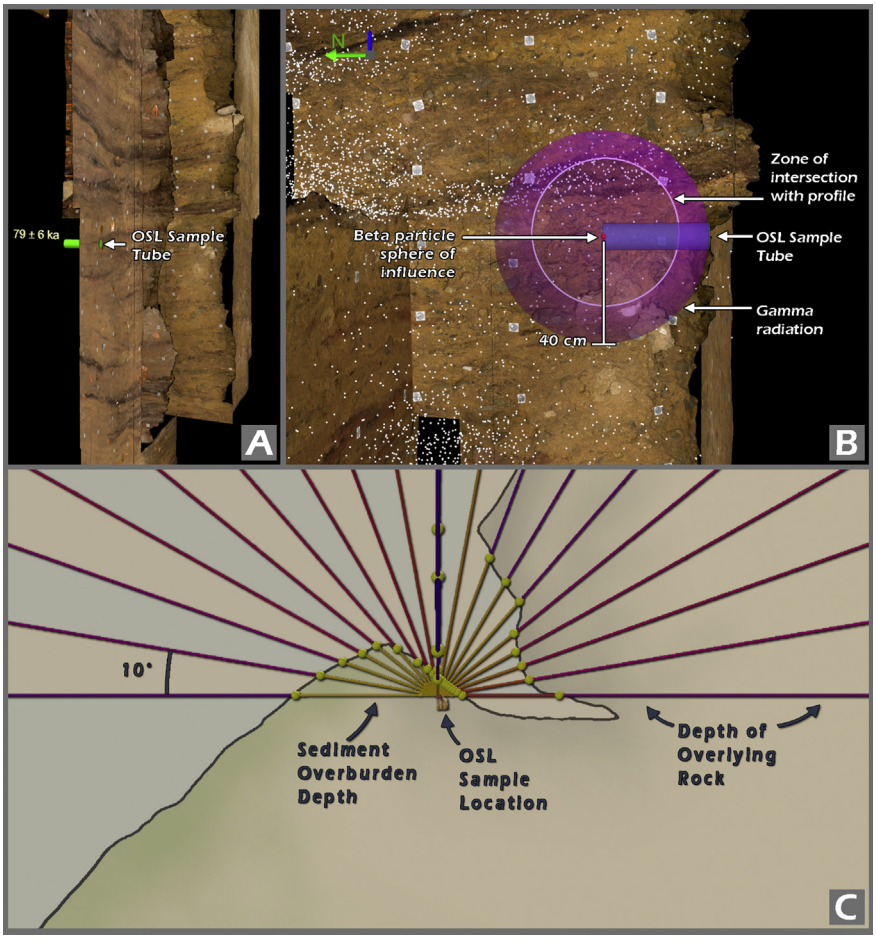

Fig. 9. Composite image showing multiple OSL samples at PP5-6 and how we use the 3D GIS and the photomosaics to model the spheres of influence for different radiation types that influence the OSL age models. (A) OSL sample 162498 showing the representation of the sample tube and the final age within the 3D GIS. (B) Diagram of OSL sample 157190 showing beta particles sphere of influence (2–3 mm radius) and gamma particles sphere of influence (30–40 cm) and the different sediments that contribute to these dose rates. (C) Profile of PP5-6 looking south showing how we calculate the amount of sediment and rock overburden that influence the cosmic dose rate.

freely at: http://www.mathworks.com/matlabcentral/fileexchange/42548.

We also used only common, industry-standard file formats. This ensured that the data would be widely supported by numerous commercial and freeware programs. There are even open-source file formats, such as Adobe Digital Negative (*.DNG), that can be substituted for proprietary file types during post-processing and used to enhance the current and long-term accessibility of the data.

The time required to use our methodology was also dependent entirely upon the field conditions and complexity of the stratigraphic sequences under study. Our experience has shown that small and easily accessible sections comprising of a half dozen photographs can be collected in under an hour. These smaller sections also do not have to be photographed at night. Most recently, we successfully collected a series of photomosaic images by draping a lightproof tarp over the immediate area that was being photographed. Care was taken to avoid light bleed and by using the maximum flash sync speed we were able to minimize the ratio of ambient light to the light generated by the flash.

Larger sections take longer to photograph, lasting several hours to several days in the most extreme cases. In these situations, the majority of time is spent on setting up the camera tripod or platform and checking focal distances, lens focus, and other parameters, and secondarily on taking the actual photographs. During our survey of the s848 section, for example, it could take over 1 h to set up and position our camera platform, which included moving the base, leveling the mast, and then reinstalling the camera equipment (which was removed for safety reasons in between moves). Thereafter, it usually took less than 20 min to photograph the entire vertical transect, which was usually comprised of ~20 images, including those for color calibration.

In general, post-processing took $2\times - 3\times$ longer than field data collection. We collected approximately 400 photographs over the span of 1 week for our s848 survey, yet it took just under one month to process the images and integrate them into our 3D GIS database. The most time-intensive process was the creation of the photomosaic warps using PTGUI. The program intuitively identified thousands of control points across overlapping images, but other key features, like our rectification chits, were not linked because they did not provide a unique enough pattern for recognition. Thus hundreds of additional control points had to be added manually to improve the mosaic accuracy. Other steps in the post-processing chain, like image and color modifications in Adobe Lightroom and cosine-fourth adjustments using Equalight, however, could be semi-automated to help speed up these tasks.

Lastly, it is worth mentioning that our methodology can also be applied to integrate previously collected imagery into photomosaics that can, in turn, be brought into a 3D database. At Site PP5-6, for example, we have begun to transform all of our older 2D georectified stratigraphic profiles into 3D profiles. Geometric and

lens effects can be removed from these older images using camera and lens profiles, but the white balance and accurate color calibrations can only be approximated because calibration targets were not used in these older photographs. Nonetheless, these images provide a useful reference because they show how the sections were excavated over time. We are now collecting all of our new imagery based on the methodology described in this paper. Our intention is to develop photomosaics of entire sections, so that the larger stratigraphic context can be studied seamlessly, and make these results reproducible and comparable to all other imagery from across the site or taken in the future.

9. Conclusions

In this paper we have described a methodology to create high-resolution, isoluminant, rectilinear, and color-corrected photomosaics of stratigraphic sections using conventional, off-the-shelf camera equipment and software. This methodology was grounded in practical photographic techniques, which can be applied to many other solutions in archaeological practice. These data have proven to be an invaluable reference to contemporary researchers, and we have provided several examples from site PP5-6 showing how the photomosaics are being used to study issues relating to site formation, geochronology, and past human behavior. Moreover, the photomosaics provide unprecedented documentation of stratigraphic profiles. It is important to preserve the fragile archaeological and sedimentological deposits found at Paleolithic and other archaeological sites. We contend that our methodology can be used to help preserve the appearance of these records for future generations of archaeological enquiry.

Acknowledgments

We thank AJ Engineering, and especially Martin Du Plessis, in Mossel Bay, South Africa for building the camera frame. We thank Robin Myers, Peter Goldstein, and Rags Gardener for their assistance and comments in helping to develop aspects of the methodology presented here. Thank you also to the entire SACP4 field team who assisted us during the collection of the imagery. SACP4 is funded by the National Science Foundation (# BCS-9912465, BCS-0130713, BCS-0524087, and BCS-1138073 to Marean), the Hyde Family Foundation, and the Institute of Human Origins (IHO) at Arizona State University. DA was funded by Grant No. NIH-NEI EY021473 to R. Rosenholtz. AIRH acknowledges funding from the Australian Research Council Discovery Grant D P0877603.

Appendix A. Supplementary data

Supplementary video related to this article can be found at http://dx.doi.org/10.1016/j.jas.2015.02.022.

References

Aitken, M.J., 1985. Thermoluminescence Dating. Academic Press, London.
Akkaynak, D., Treibitz, T., Xiao, B., Gürkan, U.A., Allen, J.J., Demirci, U., Hanlon, R.T., 2014. Use of commercial off-the-shelf digital cameras for scientific data acquisition and scene-specific color calibration. J. Opt. Soc. Am. A 31, 312–321.
Albert, R.M., Weiner, S., 2001. Study of phytoliths in prehistoric ash layers using a quantitative approach. In: Meunier, J.D., Colin, F. (Eds.), Phytoliths: Applications in Earth Sciences and Human History. Balkema Publishers, Lisse, pp. 251–266.
Albert, R.M., Marean, C.W., 2012. The exploitation of plant resources by early Homo sapiens: the phytolith record from Pinnacle Point 13B Cave, South Africa. Geoarchaeol. Int. J. 27, 363–384.
Association, A.D., 1992. TIFF: Revision 6.0. Adobe System Incoporated. http://www.adobe.com/Support/TechNotes.html.
Bar-Matthews, M., Marean, C.W., Jacobs, Z., Karkanas, P., Fisher, E.C., Herries, A.I.R., Brown, K., Williams, H.M., Bernatchez, J., Ayalon, A., Nilssen, P.J., 2010. A high resolution and continuous isotopic speleothem record of paleoclimate and paleoenvironment from 90 to 53 ka from Pinnacle Point on the south coast of South Africa. Quat. Sci. Rev. 29, 2131–2145.
Bernatchez, J., Marean, C.W., 2011. Total station archaeology and the use of digital photography. SAA Archaeol. Rec. 11, 16–21.
Bernatchez, J.A., 2008. Geochemical characterization of archaeological ochre at Nelson Bay Cave (Western Cape Province), South Africa. South Afr. Archaeol. Bull. 63, 3–11.
Binford, L.R., 1980. Willow smoke and dogs tails: hunter-gatherer settlement systems and archaeological site formation. Am. Antiq. 45, 4–20.
Brown, K.S., Marean, C.W., Herries, A.I.R., Jacobs, Z., Tribolo, C., Braun, D., Roberts, D.L., Meyer, M.C., Bernatchez, J., 2009. Fire as an engineering tool of early modern humans. Science 325, 859–862.
Brown, K.S., Marean, C.W., Jacobs, Z., Schoville, B.J., Oestmo, S., Fisher, E.C., Bernatchez, J., Karkanas, P., Matthews, T., 2012. An early and enduring advanced technology originating 71,000 years ago in South Africa. Nature 491, 590–593.
Burns, P.D., 2000. Slanted-edge MTF for digital camera and scanner analysis. In: IS and TS PICS Conference. Society for Imaging Science and Technology, pp. 135–138.
Chakrabarti, A., Scharstein, T., Zickler, T., 2009. An empirical camera model for internet color vision. In: Proceedings of British Machine Vision Conference, London, pp. 1–11.
Chandler, J.H., Bryan, P., Fryer, J.G., 2007. The development and application of a simple methodology for recording rock art using consumer-grade digital cameras. Photogramm. Rec. 22, 10–21.
CIE, C., 1932. Commission Internationale de l'Eclairage Proceedings, 1931. Cambridge University Press, Cambridge.
De Reu, J., Plets, G., Verhoeven, G., De Smedt, P., Bats, M., Cherretté, B., De Maeyer, W., Deconynck, J., Herremans, D., Laloo, P., Van Meirvenne, M., De Clercq, W., 2013. Towards a three-dimensional cost-effective registration of the archaeological heritage. J. Archaeol. Sci. 40, 1108–1121.
De Reu, J., De Smedt, P., Herremans, D., Van Meirvenne, M., Laloo, P., De Clercq, W., 2014. On introducing an image-based 3D reconstruction method in archaeological excavation practice. J. Archaeol. Sci. 41, 251–262.
Dibble, H., Marean, C., McPherron, S.P., January 2007. The use of barcodes in excavation projects: examples from Mossel Bay (South Africa) and Roc de Marsal (France). SAA Archaeol. Rec. 33–38.
Gardner, I.C., 1947. Validity of the cosine-fourth-power law of illumination. J. Res. Natl. Bureau Stand. 39, 213–219.
Goldberg, P., Berna, F., 2010. Micromorphology and context. Quat. Int. 214, 56–62.
Gonzalez-Aguilera, D., Munoz-Nieto, A., Gomez-Lahoz, J., Herrero-Pascual, J., Gutierrez-Alonso, G., 2009. 3D digital surveying and modelling of cave geometry: application to paleolithic rock art. Sensors 9, 1108–1127.
Henry, A.G., Brooks, A.S., Piperno, D.R., 2014. Plant foods and the dietary ecology of Neanderthals and early modern humans. J. Hum. Evol. 69, 44–54.
Herries, A.I.R., 2006. Archaeomagnetic evidence for climate change at Sibudu Cave. South Afr. Humanit. 18, 131–147.
Herries, A.I.R., 2009. New approaches for integrating palaeomagnetic and mineral magnetic methods to answer archaeological questions on Stone Age sites. In: Fairbrain, A., O'Conner, S., Marwick, B. (Eds.), Australian Archaeometry. The Australian National University Press, Canberra, pp. 235–253.
Herries, A.I.R., Fisher, E.C., 2010. Multidimensional GIS modeling of magnetic mineralogy as a proxy for fire use and spatial patterning: evidence from the Middle Stone Age bearing sea cave of Pinnacle Point 13B (Western Cape, South Africa). J. Hum. Evol. 59, 306–320.
Herries, A.I.R., 2014. Archaeomagnetic analysis of sediments from Djadjiling (HD07-1A-04), Jundaru (HN-A9), and HD07-3A-PAD13 rockshelters, Pilbara, western Australia (Chapter 13). In: Cropper, D. (Ed.), Rockshelter Excavations in the East Hamersley Range, Pilbara Region, Western Australia, BAR International Series.
ISO, 2009. ISO 3664:2009 Graphic Technology and Photography - Viewing Conditions. ISO, Geneva, p. 34.
Jacobs, C., 2004. Interactive Panoramas: Techniques for Digital Panoramic Photography. Springer, Berlin.
Jacobs, Z., Roberts, R.G., 2007. Advances in optically stimulated luminescence dating of individual grains of quartz from archaeological deposits. Evol. Anthropol. 16, 210–223.
Jacobs, Z., Wintle, A.G., Duller, G.A.T., Roberts, R.G., Wadley, L., 2008. New ages for the post-Howiesons Poort, late and final Middle Stone Age at Sibudu, South Africa. J. Archaeol. Sci. 35, 1790–1807.
Jensen, J.R., 2005. Introductory Digital Image Processing: a Remote Sensing Perspective, third ed. Prentice Hall, Upper Saddle River, NJ.
Karkanas, P., Bar-Yosef, O., Goldberg, P., Weiner, S., 2000. Diagenesis in prehistoric caves: the use of minerals that form in situ to assess the completeness of the archaeological record. J. Archaeol. Sci. 27, 915–930.
Karkanas, P., Shahack-Gross, R., Ayalon, A., Bar-Matthews, M., Barkai, R., Frumkin, A., Gopher, A., Stiner, M.C., 2007. Evidence for habitual use of fire at the end of the Lower Paleolithic: site-formation processes at Qesem Cave, Israel. J. Hum. Evol. 53, 197–212.
Karkanas, P., Goldberg, P., 2010. Site formation processes at Pinnacle Point Cave 13B (Mossel Bay, Western Cape Province, South Africa): resolving stratigraphic and depositional complexities with micromorphology. J. Hum. Evol. 59, 256–273.
Karkanas, P., Brown, K., Fisher, E.C., Jacobs, Z., Marean, C.W., 2015. Interpreting human behavior from depositional rates and combustion features through the study of sedimentary microfacies at site Pinnacle Point 5-6, South Africa. J. Hum. Evol. (in press).

Lerma, J.L., Navarro, S., Cabrelles, M., Villaverde, V., 2010. Terrestrial laser scanning and close range photogrammetry for 3D archaeological documentation: the Upper Palaeolithic Cave of Parpalló as a case study. J. Archaeol. Sci. 37, 499–507.
Lerma, J.L., Navarro, S., Seguí, A.E., Cabrelles, M., 2014. Range-based versus automated markerless image-based techniques for rock art documentation. Photogramm. Rec. 29, 30–48.
Lukac, R., 2008. Single-sensor digital color imaging fundamentals. In: Lukac, R. (Ed.), Single-sensor Imaging: Methods and Applications for Digital Cameras. CRC Press, Boca Raton, FL, USA, pp. 1–25.
Luo, M.R., Cui, G., Rigg, B., 2001. The development of the CIE 2000 colour-difference formula: CIEDE2000. Color Res. Appl. 26, 340–350.
Madella, M., Jones, M.K., Goldberg, P., Goren, Y., Hovers, E., 2002. The exploitation of plant resources by Neanderthals in Amud Cave (Israel): the evidence from phytolith studies. J. Archaeol. Sci. 29, 703–720.
Marean, C.W., Nilssen, P.J., Brown, K., Jerardino, A., Stynder, D., 2004. Paleoanthropological investigations of Middle Stone Age sites at Pinnacle Point, Mossel Bay (South Africa): archaeology and hominid remains from the 2000 field season. PaleoAnthropology 2, 14–83.
Marean, C.W., 2010. Pinnacle Point Cave 13B (Western Cape Province, South Africa) in context: The Cape Floral kingdom, shellfish, and modern human origins. J. Hum. Evol. 59, 425–443.
Marean, C.W., Bar-Mathews, M., Fisher, E.C., Goldberg, P., Herries, A., Karkanas, P., Nilssen, P., Thompson, E., 2010. The stratigraphy of the Middle Stone Age sediments at Pinnacle Point Cave 13B (Mossel Bay, Western Cape Province, South Africa). J. Hum. Evol. 59 (3), 234–255.
Matthews, T., Rector, A., Jacobs, Z., Herries, A.I., Marean, C.W., 2011. Environmental implications of micromammals accumulated close to the MIS 6 to MIS 5 transition at Pinnacle Point Cave 9 (Mossel Bay, Western Cape Province, South Africa). Palaeogeogr. Palaeoclimatol. Palaeoecol. 302, 213–229.
McPherron, S.J.P., 2005. Artifact orientations and site formation processes from total station proveniences. J. Archaeol. Sci. 32, 1003–1014.
McPherron, S.J.P., Dibble, H.L., Goldberg, P., 2005. Z. Geoarchaeology 20, 243–262.
McPherron, S.P., Gernat, T., Hublin, J.-J., 2009. Structured light scanning for high-resolution documentation of in situ archaeological finds. J. Archaeol. Sci. 36, 19–24.
Nikon, 2009. Specifications of the Nikon D300s Digital SLR Camera. Nikon Corp.. http://imaging.nikon.com/lineup/dslr/d300s/spec.htm
Pennebaker, W.B., Mitchell, J.L., 1993. JPEG: Still Image Data Compression Standard. Springer.
Peters, C., Church, M.J., Coles, G., 2000. Mineral magnetism and archaeology at Galson on the Isle of Lewis, Scotland. Phys. Chem. Earth A Solid Earth Geod. 25, 455–460.
Peters, C., Thompson, R., Harrison, A., Church, M.J., 2002. Low temperature magnetic characterisation of fire ash residues. Phys. Chem. Earth A/B/C 27, 1355–1361.
Remondino, F., 2011. Heritage recording and 3D modeling with photogrammetry and 3D scanning. Remote Sens. 3, 1104–1138.
Rüther, H., Chazan, M., Schroeder, R., Neeser, R., Held, C., Walker, S.J., Matmon, A., Horwitz, L.K., 2009. Laser scanning for conservation and research of African cultural heritage sites: the case study of Wonderwerk Cave, South Africa. J. Archaeol. Sci. 36, 1847–1856.
Sanger, M.C., 2015. Determining depositional events within shell deposits using computer vision and photogrammetry. J. Archaeol. Sci. 53, 482–491.
Schiegl, S., Stockhammer, P., Scott, C., Wadley, L., 2004. A mineralogical and phytolith study of the middle stone age hearths in Sibudu Cave, KwaZulu-Natal, South Africa. South Afr. J. Sci. 100, 185–194.
Shott, M., 2014. Digitizing archaeology: a subtle revolution in analysis. World Archaeol. 46, 1–9.
Sumner, T.A., Riddle, A.T.R., 2008. A virtual paleolithic: assays in photogrammetric three-dimensional artifact modelling. PaleoAnthropology 2008, 158–169.
Verhoeven, G., 2008. Imaging the invisible using modified digital still cameras for straightforward and low-cost archaeological near-infrared photography. J. Archaeol. Sci. 35, 3087–3100.
Wheatley, D., 2011. High dynamic range imaging for archaeological recording. J. Archaeol. Method Theory 18, 256–271.
Williams, D., Burns, P.D., 2007. Applying and Extending ISO/TC42 Digital Camera Resolution Standards to Mobile Imaging Products, Electronic Imaging 2007. International Society for Optics and Photonics, p. 64940H.
Wintle, A.G., Murray, A.S., 2006. A review of quartz optically stimulated luminescence characteristics and their relevance in single-aliquot regeneration dating protocols. Radiat. Meas. 41, 369–391.
X-Rite, 2012. Colorimetric Values for ColorChecker Family of Targets. XRite Photo.
Yoshida, H., Roberts, R.G., Olley, J.M., Laslett, G.M., Galbraith, R.F., 2000. Extending the age range of optical dating using single 'supergrains' of quartz. Radiat. Meas. 32, 439–446.